

Full Length Research Paper

Downscaling Albedo from moderate-resolution imaging spectroradiometer (MODIS) to advanced space-borne thermal emission and reflection radiometer (ASTER) over an agricultural area utilizing ASTER visible-near infrared spectral bands

Mohammad H. Mokhtari^{1,2*} and Ibrahim Busu¹

¹Department of Remote Sensing, Faculty of Geo-information Science and Engineering, University Technology of Malaysia (UTM), Malaysia.

²Faculty of Natural Resources, Yazd University, Iran.

Accepted 27 September, 2011

Due to the limitation in spatial and spectral resolution, a few numbers of satellite data are applicable in field scale surface Albedo modeling. ASTER was an alternative for surface energy balance modeling, but since April 2008, shortwave detector has stopped recording due to the high-abnormal-temperature problem. Beside, temporal resolution of ASTER is insufficient for field-scale monitoring of surface parameters. Thus, this study was aimed first; to examine the capability of ASTER VNIR bands in estimation of surface Albedo and second, to downscale Albedo from MODIS to ASTER using Albedo resulted from ASTER VNIR bands. Combination of these two stages is expected to be a solution for field scale monitoring of surface Albedo from MODIS and ASTER data acquired after April 2008. Results confirmed that bands 1 and 3 which is available after April 2008 on ASTER data can be modeled for estimation of surface Albedo with less than 0.024% loss of information where land cover consist of soil and vegetation. From four downscaling methods, namely FSIM, PBIM, wavelet transfer and high pass filter (HPF) examined in this study, we also found that the most precise subpixel estimate were obtained by FSIM downscaling method ($R^2 = 0.96$, RMSE = 0.01); although, the outputs of three other methods were significant.

Key words: Albedo, downscaling, moderate-resolution imaging spectroradiometer (MODIS), advanced space-borne thermal emission and reflection radiometer (ASTER), multiple regression, wavelet, high pass filter (HPF), pixel block intensity modulation (PBIM), filter-based intensity modulation (FSIM).

INTRODUCTION

As a result of technical satellites constraints, it is difficult to find data relatively with both high spatial and temporal resolution properties for land surface studies. Therefore, low spatial resolution data in many cases are converted to the scale of high spatial resolution to obtain detail information in the required scale by using scaling methods, particularly when heterogeneous surfaces in

relative to the pixel size is considered. Thus, subpixel information of mixed pixels which are contained in several land cover type is essential when the high spatial resolution image is not available for a period of time or is limited due to its low temporal frequency.

Combination of various spatial and temporal resolution images has been identified to be a solution for determination of spatio-temporal characteristics of land surface parameters of heterogeneous area (Saura and Castro, 2007). However, different characteristics of various scaling methods have increased the efforts on the way of developing proper practical scaling methods for

*Corresponding author. E-mail: mokhtari.mh@gmail.com. Tel: +60 173472496.

relocating patterns of surface parameters across different spatial resolution (Saura, 2004). Since images from different sensors of the same satellite or different satellite can be acquired of the same area and at comparable time and date, several studies, such as derivation of landscape pattern metrics for the assessment of land cover condition and landscape change dynamics by means of advanced very high resolution radiometer (AVHRR), LANDSAT, SPOT and aerial photograph data (Saura and Castro, 2007), increase the spatial resolution of the multispectral wavebands of thematic mapper (TM) data to pixel size of PAN image (Pardo-Iguzquiza and Atkinson, 2007), similarity assessment of satellite and ground-based normalized difference vegetation index (NDVI) (Wang et al., 2004), air temperature parameterization by means of SEVIRI and MODIS data (Zaksek and Schroedter-Homscheidt, 2009), downscaling MERIS data to LANDSAT-like resolution data for monitoring vegetation seasonal dynamic (Zurita-Milla et al., 2009), crop type distribution using temporal unmixing (Ozdogan, 2009), estimation of temporal and spatial distribution of evapotranspiration in field scale (Kaheil et al., 2008; Kustas et al., 1994; Ozdogan, 2009) and estimation of subpixel vegetation water content using MODIS and LANDSAT data (Huang et al., 2009) have attempted to estimate land surface parameter through scaling functions from the coarse mixed pixels. The effect of various scaling function from simple linear based models, such as smoothing filter-based intensity modulation (SFIM) (Liu, 2000), pixel block intensity modulation (PBIM) (Guo and Moore, 1998), RGB to HIS transform (Haydan et al., 1982) to the more complicates based on signal decomposition, such as wavelet transfer (Burrus et al., 1998; Gangkofner et al., 2008) and co-kriging (Pardo-Iguzquiza et al., 2006) have been reported by several authors (Benson and MacKenzie, 1995; Griffith et al., 2003; Kojima et al., 2006; Pardo-Iguzquiza et al., 2009; Yu and Ng, 2006).

Albedo is defined as total hemispherical reflectance integrated over all angles of the upward hemisphere (Pinker and Stowe, 1990). Since reflectance measurement in all angle of the upward hemisphere is difficult, it is assumed to be equivalent to the nadir reflectance factor (Ranson et al., 1991). Estimation of spatial and temporal variation of land surface Albedo is necessary for shortwave budget computation and environmental studies (Bhattacharya et al., 2009; Ranson et al., 1991); therefore, several studies have attempted to estimate Albedo from bi-directional reflectance measurements by different data sources (Kimes and Sellers, 1985; Kriebel, 1979; Ranson et al., 1991; Walthall et al., 1985). Recently, researchers have began to obtain surface Albedo from satellite images (Hong et al., 2009). However, detected apparent reflectance by the remotely sensing sensors is affected by instrument field of view, viewing geometry, meteorological conditions and atmospheric optical parameters (Pinker and Stowe,

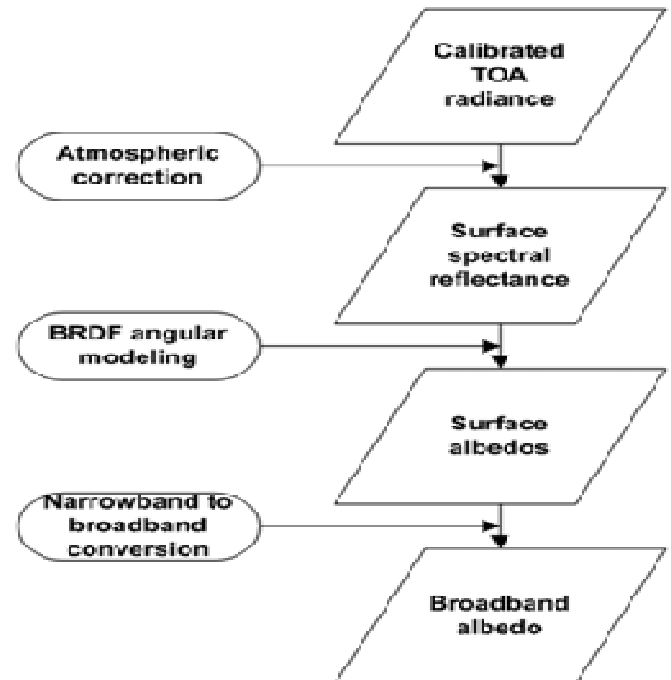


Figure 1. A scheme of converting TOA radiance to broadband Albedo (Liang et al., 2003).

1990). As a result, accurate information about atmospheric condition and land surface characteristic are necessary (Liang et al., 2003).

Satellite sensors are built to measure narrowband at the top of atmosphere; therefore, the following approaches have been proposed to determine surface broadband Albedo from measured narrowband; first, estimation of Albedo directly from top of atmosphere (TOA) radiance by extensive radiative transfer simulation and then, linking simulated TOA reflectance with surface broadband Albedo using nonparametric regression algorithm. Second, NASA MODIS science team approach (Schaaf et al., 2002) as shown in Figure 1.

The weighting factors for spectrally integrated narrowband reflectance data have been estimated and validated for different satellite data, such as ALI, AVHRR, ASTER, geostationary operational environmental satellite (GEOS), MISR, MODIS, POLDER, LANDSAT TM/ETM and VEGETATION (Liang et al., 2003).

Due to limitation in spatial and spectral resolution, a few number of aforementioned satellite data are applicable in field scale (~10 to 200 ha) modeling of land surface parameters. Among the currently operating satellites data, moderate resolution data has been recognized as key factor in land surface parameter estimation through space (Folhes et al., 2009). LANDSAT with a moderate spatial resolution is the most used satellite data owing to its systematic data acquisition as well as global coverage. However, the near future

operation of LANDSAT is reported to be uncertain. Similar to LANDSAT, advanced space-borne thermal emission and reflection radiometer (ASTER) as an alternative was used in field scale applications. ASTER was provided by the Japanese Ministry of International Trade and Industry to the National Aeronautics and Space Administration (NASA) and was launched on the 18th December 1999 as part of NASA's earth observing system (EOS)-AM1 spacecraft (Abrams, 2000). The sensor covers visual and near infrared (VNIR) with three bands at 15 m spatial resolution (but lacking coverage in the blue region), the shortwave infrared (SWIR) with six bands at 30 m spatial resolution and the thermal infrared (TIR) region of electromagnetic spectrum with five bands at 90 m (Fujisada and Ono, 1991). The sensor provides backward VNIR band (3B) which can be used for producing digital elevation model. Regrettably, since April 2008, shortwave of ASTER detector has stopped and data acquired after April 2008 were invalid due to the high-abnormal-temperature problem of SWIR detector. This problem has made ASTER data ineffective in estimation of surface Albedo and therefore, energy balances modeling (ERSDAC, 2010).

In addition, the utilization of LANDSAT and ASTER in land surface studies and monitoring is restricted by their low temporal resolution. Nevertheless, availability of both ASTER high and MODIS moderate spatial resolution data at the same overpass time (as they are mounted on platform, Terra) is the advantage of using these data for field scale monitoring of land surface parameter as well as surface Albedo's. As mentioned earlier, Albedo varies as function of solar zenith angle and atmospheric visibility which are time dependant variables (Grant et al., 2000). The effects are almost similar on both data acquired by the same satellite at the same time; thus, data assimilation processes are reduced or in some cases can be eliminated when these data are integrated. Moreover, simultaneity characteristic of these sensors reduces complex image pre-processing procedures, such as relative radiometric correction or radiometric normalization as they are essential in the case of using multiple satellite images with different overpass time (Canty et al., 2004).

This study is aimed first; to explore the capability of ASTER VNIR and SWIR spectral bands (except thermal bands) in estimating surface Albedo using statistical approach. Therefore, the most dominant spectral bands in estimation of surface Albedo as well as VNIR bands will be considered and modeled. Second, to downscale Albedo estimated from MODIS to ASTER using Albedo image obtained from the first step. Four downscaling methods, namely SFIM, wavelet, HPF and PBIM were considered. Albedo image of ASTER data computed through the model presented by Liang (2004) which utilizes both VNIR and SWIR spectral bands will be considered as reference in this study. Thus, the combination of the aforementioned method is expected to be a solution for field scale monitoring of surface Albedo

from the ASTER and MODIS data acquired after April 2008.

Study area description and data set

The area under study is Bahadoran agricultural area, located in the Southern region of Mehriz district, Iran, between 31.28 and 31.48 N and 54.80 and 55.00 E (Figure 2). According to Domarton classification method, its climate is semiarid. The most abundant land cover classes in the analyses subset were perennial Pistachio trees and bare soil. Therefore, selection of such area with fixed land cover type possesses an advantage that makes it an appropriate choice for validating the models over the time.

Table 1 illustrates the satellite data utilized in this study, which includes cloud free ASTER images acquired before April 2008. The reason of selecting the data before April 2008 was due to normal acquisition of ASTER data in all visible-near infrared and shortwave infrared, which allow the comparison of estimated Albedo from both with and without shortwave spectral bands. Consequently, as an advantage, direct quantification of the quality is allowed. It should be noted that evaluation and validation of original model which uses VNIR and SWIR bands for estimation of surface Albedo is out of the scope of this paper.

MATERIALS AND METHODS

In the first step, the capability of ASTER VNIR and SWIR spectral bands were evaluated statistically using the image taken on day 186 of year 2000. Albedo was estimated from pre-processed VNIR ASTER spectral bands and then, four downscaling methods, namely FSIM, PBIM, HPF and wavelet transfer were examined using MODIS and ASTER co-registered images. Finally, the performances of these methods were evaluated statistically. Capability of VNIR-based Albedo as well as downscaled images was evaluated based on the reference image computed from Equation 1 that utilizes ASTER VNIR and SWIR spectral bands.

Images and pre-processing

Two sets of satellite data including ASTER and MODIS images were analyzed in this study. Cloud-free ASTER Level 1B image was obtained for estimation of Albedo (Table 2). The Level 1B ASTER data presents radiance at sensor ($Wm^{-2}sr^{-1}\mu m^{-1}$) and it is produced from level 1A reconstructed and unprocessed data by applying radiometric coefficient. As it is necessary to remove the effects of changes in sun-satellite geometry and aerosol scattering, atmospheric correction was performed on solar reflective (VNIR and SWIR) bands of both ASTER and MODIS data to provide radiation reflected at the surface (Abrams, 2000; Kimes and Sellers, 1985). The atmospheric correction of ASTER data requires outside sources for atmospheric correction, since the system was not designed to repossess atmospheric information. In this study, fast Line-of-sight analysis of spectral hypercubes (FLAASH) on ASTER VNIR and SWIR bands was performed using climatic parameter

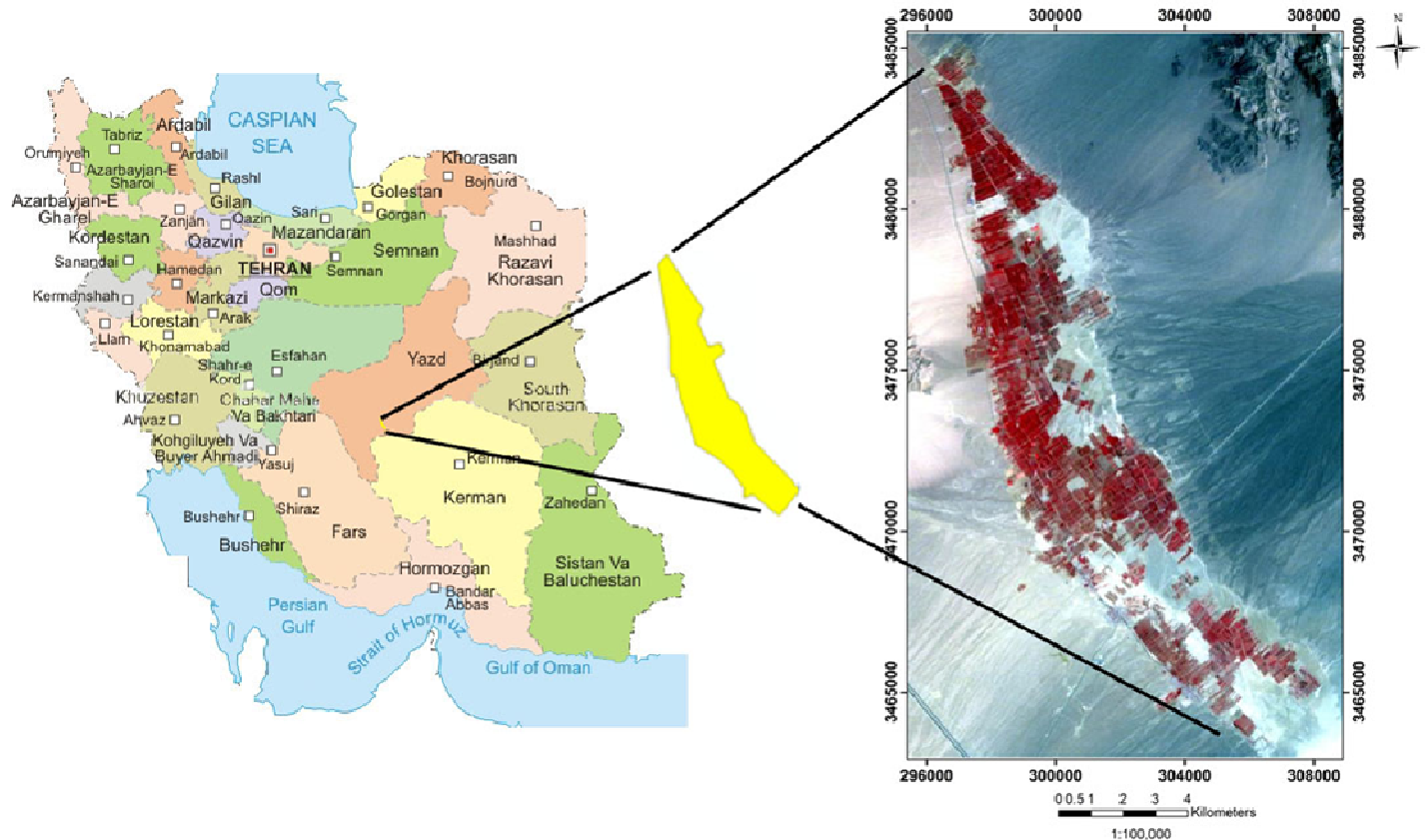


Figure 2. Location of study area (Right image: ASTER, RGB: 3, 2 and 1).

Table 1. Satellite data of the study.

Image	Data level	Overpass time (UTC)	Year-Julian day
ASTER	L1B	7.29	2000 - 186
MODIS	L1B	Starting: 7.25, ending: 7:29	2000 - 186

Table 2. Estimated regression coefficients (Dependent Variable: MODIS 500 m Albedo).

Data	Unstandardized coefficients		Standardized coefficients		t	Sig.
	B	Standard error	Beta			
Constant	0.035	0.003	-		11.954	0.000
ASTER	0.899	0.011	0.925		83.974	0.000

and atmospheric modeling. The output then was converted to the reflectance using the radiative transfer codes (atmospheric modeling). In this method, atmospheric water vapor from spectral bands of 0.94 to 1.14 μm is calculated and atmospheric scattering is modeled. Via this process at sensor radiance is converted to the at-surface reflectance (Gupta, 2003). ASTER image was geo-referenced to the UTM/WGS84 zone number 40 by the collected 25 dispersed ground control points (GCPs). Then, MODIS image was co-registered to the ASTER data taken on the same date. Accuracy of the geo-referencing was evaluated by calculation of root mean square error (RMSE < 0.32). As the last pre-processing step, the

area of interest which covers Bahadoran agricultural area was extracted from both ASTER and MODIS data scenes. The ASTER and MODIS images acquired on day 186 of year 2000 were used for multiple regression analysis and downscaling, respectively. In this study, narrowband reflectance of ASTER and MODIS VNIR and SWIR spectral bands were converted to broadband Albedo using the models presented by Liang (2004). These models were generated for different satellite sensors by extensive radiative transfer simulation and using atmospheric radiative transfer (SBDRT) codes (Ricchiazzi et al., 1998). The proposed models for ASTER and MODIS consist of six independent variables (VNIR and

SWIR bands) as follows (Liang, 2004):

$$\alpha_{ASTER} = 0.484\alpha_1 + 0.335\alpha_3 - 0.324\alpha_5 + 0.551\alpha_6 + 0.305\alpha_8 - 0.367\alpha_9 \quad (1)$$

$$\alpha_{MODIS} = 0.16\alpha_1 + 0.291\alpha_2 - 0.243\alpha_3 + 0.116\alpha_4 + 0.112\alpha_5 - 0.081\alpha_7 \quad (2)$$

where α is the surface Albedo and α_1 through α_n are the ASTER and MODIS spectral bands in reflectance.

Multiple regression analysis

In order to explore the contribution of each ASTER spectral band(s) and their potential in predicting surface Albedo, multiple regression analysis was performed and new regression equation was established using bands with larger contribution. Hence, the effects of presented bands in Equation 1 as well as band number 2 (which is available on data taken after April 2008) in estimation of Albedo were considered.

Initially, bivariate correlation analysis was performed based on Pearson product-moment correlation coefficient to examine the strength and direction of the relationship between ASTER spectral bands and estimated Albedo through the model presented by Liang (2004) as well as exploring the amount of variance of Albedo accounted for by each spectral band. The relationship between dependent and independent variables were visually inspected. The incorporated analysis of seven ASTER spectral bands (band numbers 1, 2, 3, 5, 6, 8 and 9) was performed for predictive calculations of surface ALBEDO through multiple regression analysis to evaluate the amount of Albedo variances explained by ASTER spectral bands. Thus, the values of the aforementioned spectral bands were entered in the regression equation and significance of inter-relationship between variables including, dependent and independent were evaluated based on yielded prediction of each band in regard to the predictability of other spectral bands. Then, fundamental ASTER bands that present the patterns of correlations within a set of ASTER data bands, contributing in the estimation of surface Albedo were determined. A general form of linear regression model is presented as follows:

$$Y_i = \beta_0 + \sum_{j=1}^n \beta_j X_j + \varepsilon_i \quad (3)$$

where Y_i is i^{th} of dependent variable (DV) (Albedo), β_0 is line interception coefficient, β_i is regression coefficients of i^{th} independent variable IV (ASTER spectral bands), that are determined by fitting the equation to the data, X_1 through X_n are the independent variable (ASTER spectral bands) and ε presents the difference between observed and predicted value of DV.

The total variability of dependant variable accounted for by multiple linear regression was measured through coefficient of determination as follow (Tabachnick and Fidell, 2007):

$$R^2 = \frac{SS_{reg}}{SS_y} \quad (4)$$

$$SS_y = \sum (y - \bar{y})^2, \quad SS_{reg} = \sum (y' - \bar{y})^2 \quad (5)$$

where SS_y is the total sum of squares difference between each observed value y and the mean of y over all cases and SS_{reg} is the total sum of squared due to regression calculated from predicted value (y') and the mean of y over all cases.

The squared multiple correlation was also calculated from the sum of the correlation between dependent and independent variable, r_{y_i} and standardized regression coefficient, β_i of independent variable as follows:

$$R^2 = \sum_{i=1}^k r_{y_i} \beta_i \quad (6)$$

where r_{y_i} is the correlation between dependent variable and i^{th} independent variable and β is the standardized regression coefficient that is used to estimate standardized y' .

Unstandardized coefficient was obtained by converting standardized coefficient through the following equation:

$$B_i = \beta_i \left(\frac{S_y}{S_i} \right) \quad (7)$$

where B_i is the unstandardized coefficient, S_i is the standard deviation of i^{th} independent variable, S_y is the standard deviation of dependent variable. Finally, an intercept, β_0 was calculated once the unstandardized coefficient had been determined:

$$\beta_0 = \bar{y} - \sum_{i=1}^k (B_i \bar{X}_i) \quad (8)$$

The model presented in Equation 1 was used to estimate surface Albedo from pre-processed ASTER data acquired on the 4 of July 2000. Then, Albedo as a dependent variable and raster sets of bands number 1, 2, 3, 5, 6, 8 and 9 (reflectance values) as independent variables were analyzed statistically. Each layer consists of 513,608 numbers of points. Pixel values of each raster set were converted to data base format (DBF) to be analyzed with statistical software's.

In addition, preliminary data analysis was performed to evaluate multi collinearity, normality, linearity, homoscedasticity and independence of residuals of variables. Subsequently, forward regression analysis was conducted to consider the potential of particular ASTER bands in predicting Albedo when the effects of other bands are controlled. The method starts selecting band which can explain the most variance of independent variable. Then, the second most influential band was selected and remodeled; it was continued until all variances of Albedo are accounted for by the model. All predictive models of selected bands were generated via step-wise forward regression analysis. Evaluation of the most appropriate model was performed by plotting this model against the Albedo computed from Equation 1 and calculating correlation coefficients.

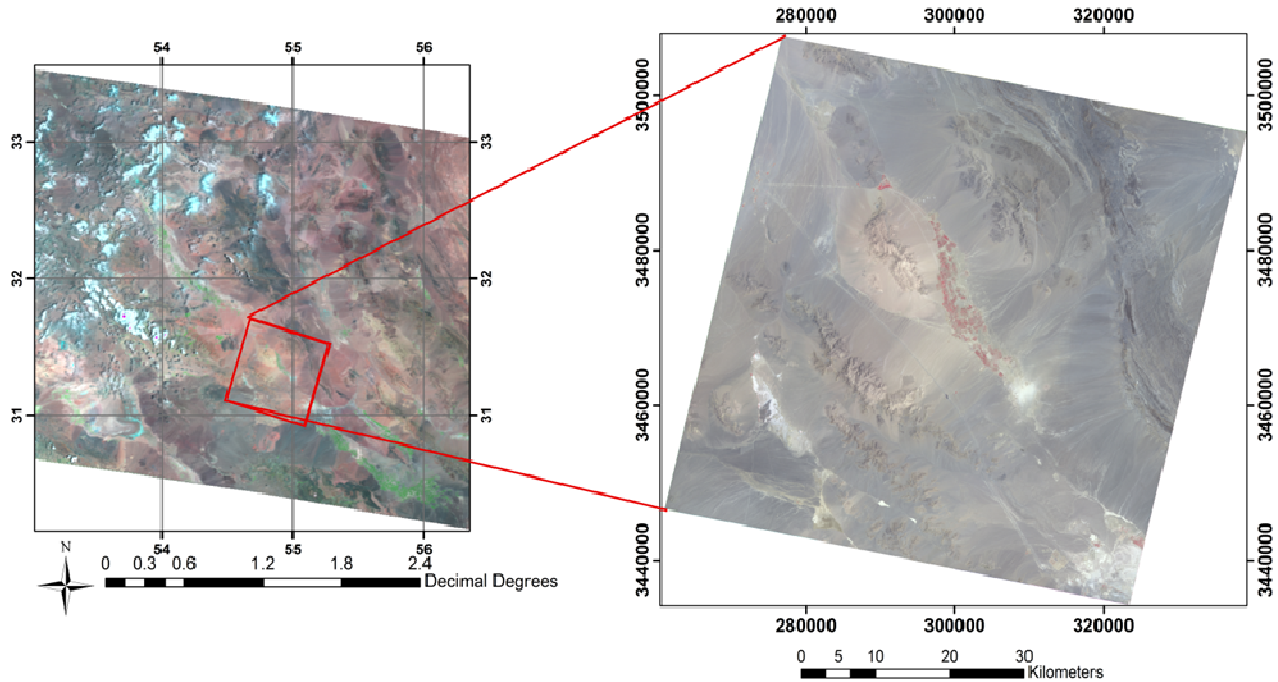


Figure 3. The location of study area on ASTER data scene (FCC: 3, 2 and 1) (right) and MODIS image (FCC: 7, 2 and 1) (left) taken on the same date and time.

Downscaling Albedo

Revisit time of ASTER data is 16 days, because of small sensor's field of view (60×60 km); in many cases it is difficult to find an image that takes each sixteenth day from the same area. In addition, this image acquisition frequency is insufficient, normally for monitoring land surface parameter, such as Albedo, and as a result for energy balance modeling. Thus, combinations of ASTER derived land surface parameters with higher temporal resolution data is required for land surface parameters monitoring. Consequently, combination of MODIS as a high temporal resolution (1 to 2 days revisit time) and ASTER data with their sensors that have been mounted on the same platform (Terra) is expected to retain detail information of land surface Albedo. According to MODIS image acquisition start time (7.25 am), time of its ending (7.29 am) and location of the study area which has been positioned at the middle (horizontally) of the image scene. Study area part of the MODIS image has been taken around 7.27 am. Therefore, the acquisition time difference between MODIS and ASTER image is expected to be about 1 to 2 min. Thus, two images were taken in similar solar illumination conditions and the same viewing angle since both sensors have been located at the same observing point. Figure 3 shows the study area on both ASTER and MODIS images.

In this study, Albedo images were calculated from MODIS data using VNIR-SWIR bands and ASTER VNIR bands using the model created via regression analysis. Then, four image downscaling method, including smoothing filter-based intensity modulation (FSIM), pixel block intensity modulation (PBIM), wavelet transfer and high pass filter (HPF) were utilized to downscale Albedo from MODIS to ASTER data. The results were evaluated by comparing the output of each method with reference Albedo image computed from ASTER image via Equation 1.

PBIM and FSIM can be applied on individual bands and simulated image retains original characteristic of low resolution image. In addition, the spectral properties of the simulated image

are independent of the high-resolution image (Liu, 2000; Stathopoulou and Cartalis, 2009).

Since Albedo image of both MODIS and ASTER were used for downscaling, these images were spectrally identical. This met the assumption of the algorithms of the selected models; therefore, comparison of the methods is facilitated.

As it is prerequisite for data scaling, pre-processed MODIS and ASTER images acquired on the 4 of July 2000 were co-registered accurately to a common coordinate reference system. Nearest neighborhood algorithm was selected as resampling method that results better protection of the original pixel value relative to other methods. This method uses nearest pixel as the label for registered pixel, but linear features are split between lines by this method. However, this method was suggested for image processing, if the most information is required to be extracted from images (Congalton, 2010). Then, Albedo images generated from Equation 2 for MODIS (Liang et al., 2003) and Equation 9 for ASTER (generated via regression analysis of ASTER VNIR bands) were used for downscaling. In order to combine estimated Albedo in 15 m resolution with 500 m coarse data, ASTER Albedo image was degraded to 50 m (the minimum possible size to create an image with fraction of 500 m) spatial resolution to be a fraction of 500 MODIS image using a real averaging approach. This spatial size is applicable for the study area since typical length scales of features is greater than 250 m and as a result, truthful characterization of heterogeneity is possible. Thus, 10 by 10 block of ASTER pixels were fitted exactly into a single MODIS pixel.

$$\alpha_{ASTER_REG} = 0.696\alpha_1 + 0.299\alpha_3 + 0.008 \quad (9)$$

where α_1 through α_3 are the ASTER spectral bands in reflectance, α_{ASTER_REG} is the Albedo modeled by regression

Table 3. Descriptive statistics of MODIS 500 m resolution image and aggregated ASTER 50 to 500 m resolution.

Data	N	Minimum	Maximum	Mean		Standard deviation		Variance		Skewness		Kurtosis	
	Statistic	Statistic	Statistic	Statistic	Standard error	Statistic	Statistic	Statistic	Standard error	Statistic	Standard error	Statistic	Standard error
MODIS	1188	0.1158	0.3481	0.27587	0.00069	0.02387	0.001	-0.160	0.071	2.082	0.142		
ASTER	1188	0.1002	0.3439	0.26855	0.00071	0.02458	0.001	-0.288	0.071	1.941	0.142		

analysis.

PBIM method

Linear unmixing method has been recommended for combination of information when high and a low spatial resolution image are simultaneously available over a particular area. Beside, signals identification of individual component in the mixed pixel is unnecessary in linear based data fusion models (Zurita-Milla et al., 2009). Thus, PBIM (Guo and Moore, 1998), (Equation 19) as a linear model was selected since Albedo can be estimated similarly from both ASTER and MODIS images. Ability in merging images with different spatial resolution from different sensors, application in individual bands and retaining the radiometric characteristic of the original low spatial resolution image are the advantage of using this method in combining high and low spatial resolution data (Stathopoulou and Cartalis, 2009). The PBIM downscaling procedure consists of the following stages:

1. ASTER Albedo image was degraded to the resolution of MODIS image (500 m) using pixel averaging approach.
2. In order to obtain linear regression model, degrade ASTER image in 500 m spatial resolution was crossed with MODIS Albedo 500 resolution image. As illustrated in Figure 4, a correlation coefficient of 0.856 was found in regression between two images. The estimated regression coefficients between ASTER and MODIS 500 m resolution and the description statistic of the images in this step are illustrated in Tables 2 and 3, respectively.

Once the parameters of regression line were determined, they were applied to the ASTER data with 50 m spatial resolution to estimate corresponding Albedo in high resolution. Thus, simulated subpixel value of the MODIS is determined as follows:

$$Albedo_{MODIS\ 500m} = \alpha + \beta Albedo_{ASTER\ 500m} \quad (9)$$

$$Albedo_{Simulated_MODIS50m} = \alpha + \beta Albedo_{ASTER50m} \quad (10)$$

where $\alpha = 0.035$ and $\beta = 0.899$ in this study.

As final step scaling factor, the model is calculated as follows:

$$Albedo_{MODIS50m} = \frac{Albedo_{MODIS500m} \cdot Albedo_{Simulated_MODIS50m}}{Albedo_{Simulated_MODIS500m}} \quad (11)$$

where $Albedo_{MODIS\ 500m}$ is the Albedo image estimated from MODIS data in 500 m spatial resolution and $Albedo_{Simulated_MODIS\ 50m}$ is the simulated image calculated from Equation 10.

Smoothing filter-based intensity modulation (SFIM)

SFIM method has been developed by Liu (2000) based on simplified solar radiation and land surface reflection model. This method downscale the image by using a ratio between a higher resolution image and its low pass smoothing filtered image to retrieve detail information from low spatial data. It has been reported that this method does not distort the spectral properties and image contrast. It can either be applied on multi-spectral bands or single images in order to enhance spatial detail. The comparison of SFIM with HIS and Brovey transform outputs have indicated better enhancement of spatial detail of multi-spectral image by FSIM over the HIS and Brovey transform methods. As the other downscaling methods, FSIM is sensitive to the quality of co-registration of high and low spatial image. However, the effect of error of co-

registration (blurred feature and mismatched edge in downscaled image) can be reduced by using larger kernel size than the resolution ratio of low and high spatial image. The summary of the method for downscaling of single image is presented as follows (Liu, 2000):

$$HighR_{Downscaled} = \frac{image_{low} * image_{high}}{image_{mean}} \quad (12)$$

where $HighR_{Downscaled}$ is the high resolution downscaled image, $image_{low}$ is a pixel of a lower resolution image co-registered to a higher resolution image of $image_{high}$, $image_{mean}$ is a smoothed pixel of $image_{high}$ using averaging filter over a neighborhood equivalent to the actual resolution of $image_{low}$.

Preliminary averaging filter is defined as a based resolution ratio of high spatial and low spatial resolution images and it is optimized by the correlation between SFIM image and high and low spatial resolution images. In this study, a smoothing filter kernel of 10×10 (50 m high resolution ASTER Albedo and 500 m low resolution MODIS Albedo) were selected in the SFIM method.

Wavelet transform method

Wavelets are defined as small wave location and varying features that can be presented by their energy (Burrus et al., 1998; Gangkofner et al., 2008). It is based on decomposition of the image into several channels with different resolution by their local frequency content. Wavelet transfer method has been used by several researchers to

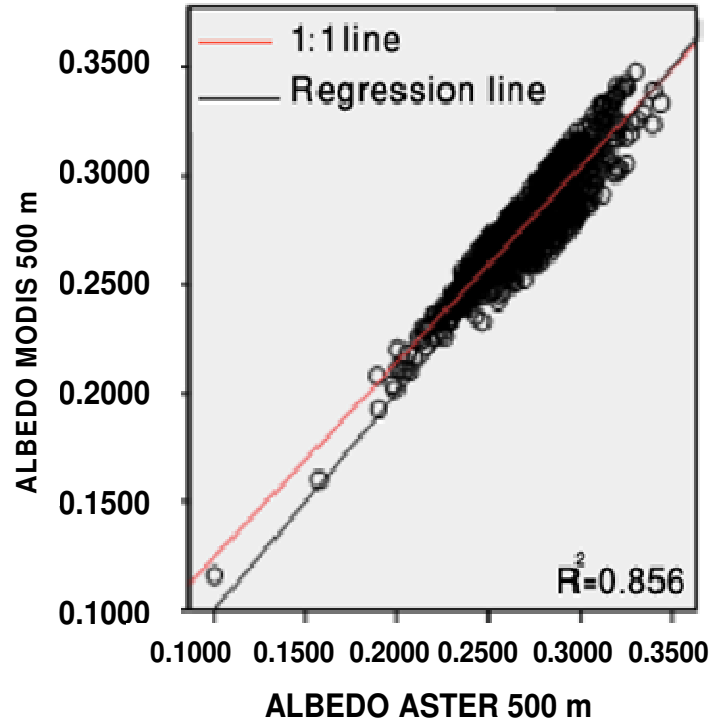


Figure 4. Graph of correlation between ASTER Albedo aggregated to 500 m and MODIS 500 m resolution Albedo image.

to fuse satellite images with different spatial resolution, and the results have usually shown that wavelet transform functions improve the spatial resolution with minimum distortion of the spectral content of the original image (Ranchin et al., 2003; Shi et al., 2005; Shi et al., 2003; Yocky, 1996). The method can either be applied to merge a panchromatic band with multi spectral data (multi-band wavelet) or combine two gray scale images (two-band wavelet) (Bruno et al., 1996). Once the basic waveform is defined, the image can be decomposed by applying coefficients to each of the waveforms. Given a sufficient number of waveforms, all the detail in the image can be defined by coefficient multiples of the ever-finer waveforms. This method uses short and discrete wavelet transform (DWT) instead of long continuous wave (sine and cosine) (Strang and Nguyen, 1996). Shift-variant discrete wavelet decomposition (DWT) has identified suitable method for signal analysis and pattern recognition as compared to other methods, such as orthonormal. Thus, in this study, shift-variant discrete wavelet decomposition method was performed using four-order decomposition and reconstruction spline biorthogonal wavelet. As it is illustrated in Figure 5 in practice, four images are produced through discrete wavelet transform procedure from high spatial resolution image (Gonzalez et al., 2004; King and Wang, 2001):

1. Approximation coefficients (A): the low-pass image.
2. Horizontal coefficients (H): details along the columns.
3. Vertical coefficients (V): details along the rows.
4. Diagonal coefficients (D): details along the diagonals.

The following steps are used in wavelet transfer method for image fusion:

1. Decomposition of fine resolution ASTER Albedo image into a set of ASTER coarse resolution images with wavelet coefficients.
2. Replacement of generated low resolution from the previous stage with MODIS coarse pixel Albedo at the same level.

3. Applying reverse wavelet transformation with corresponding V, D and H image produced from previous stage to produce linear intensity image in order to convert decomposed and replaced Albedo of ASTER to the pixel size of high resolution image.

HPF method

High pass filter (HPF) method allows the combination of high resolution data with low resolution multi spectral data from the same or different sensors. The method involves a convolution using a high pass filter on the high resolution data, then combining this with the lower resolution data. The first step is the application of high pass filter to determine the R value; the ratio of the low resolution image to pixel size of high resolution in this study is set to 10. Then, center value of the filter is determined based on the R value and other values of the filter are set to -1. Table 4 illustrates a set of parameter used in HPF methods.

The second step is the high pass filter of the high resolution image. In order to apply high pass filter result, low resolution image is resampled to the pixel size of high resolution image using bilinear algorithm. Then, HPF image (new low spatial image) is stretched to match the mean and standard deviation value of the original low resolution image. For this, a weighing function is used as follows:

$$W = \frac{SD_{MS}}{SD_{HPF} * M} \quad (13)$$

where W is the weighting multiplier for HPF image value. SD_{MS} is the standard deviation of the low spatial resolution image to which the high pass filter image is being added. SD_{HPF} is the standard deviation of the high pass filter image. M is the modulating factor to determine the crispness of the output image based on R value as

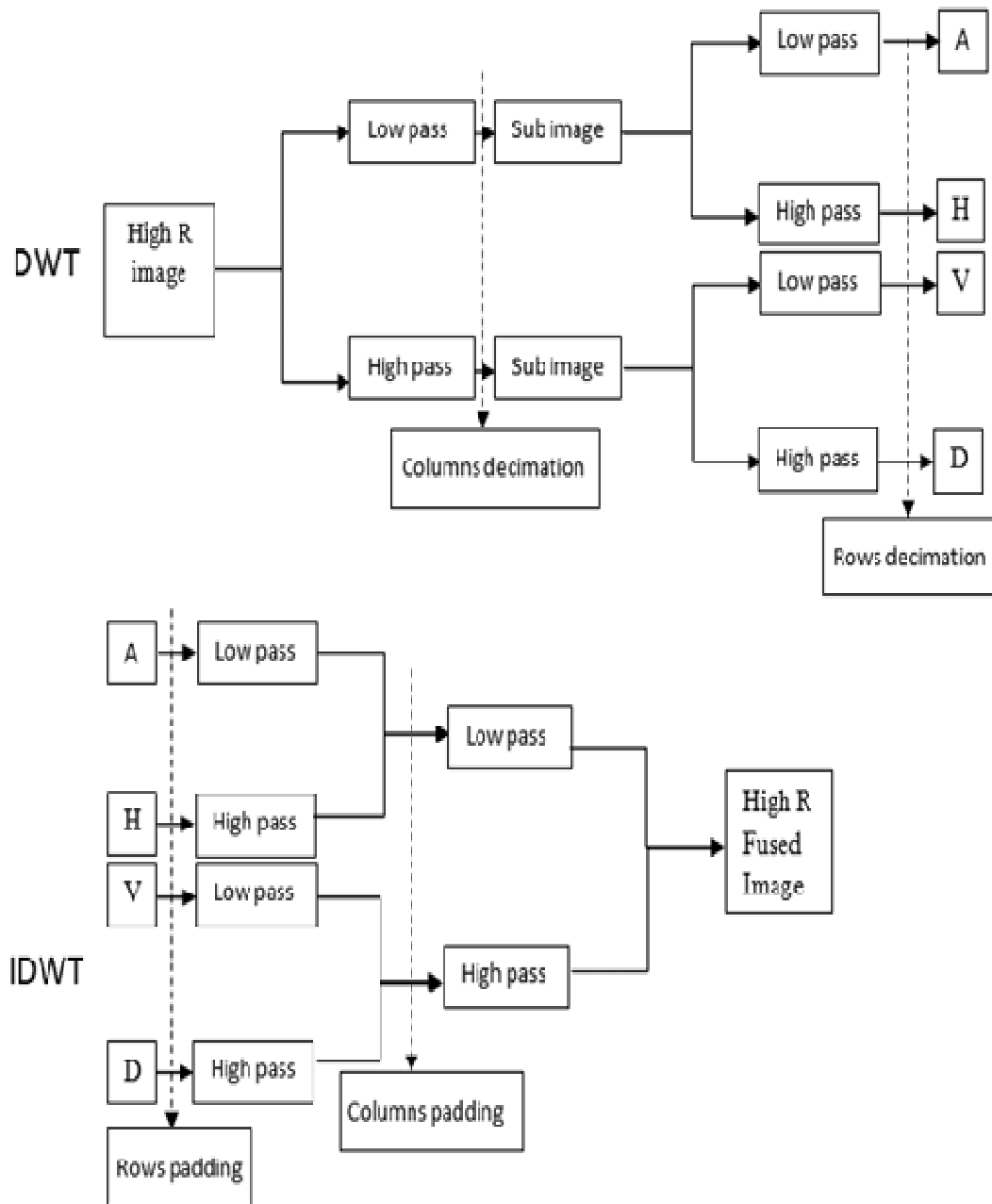


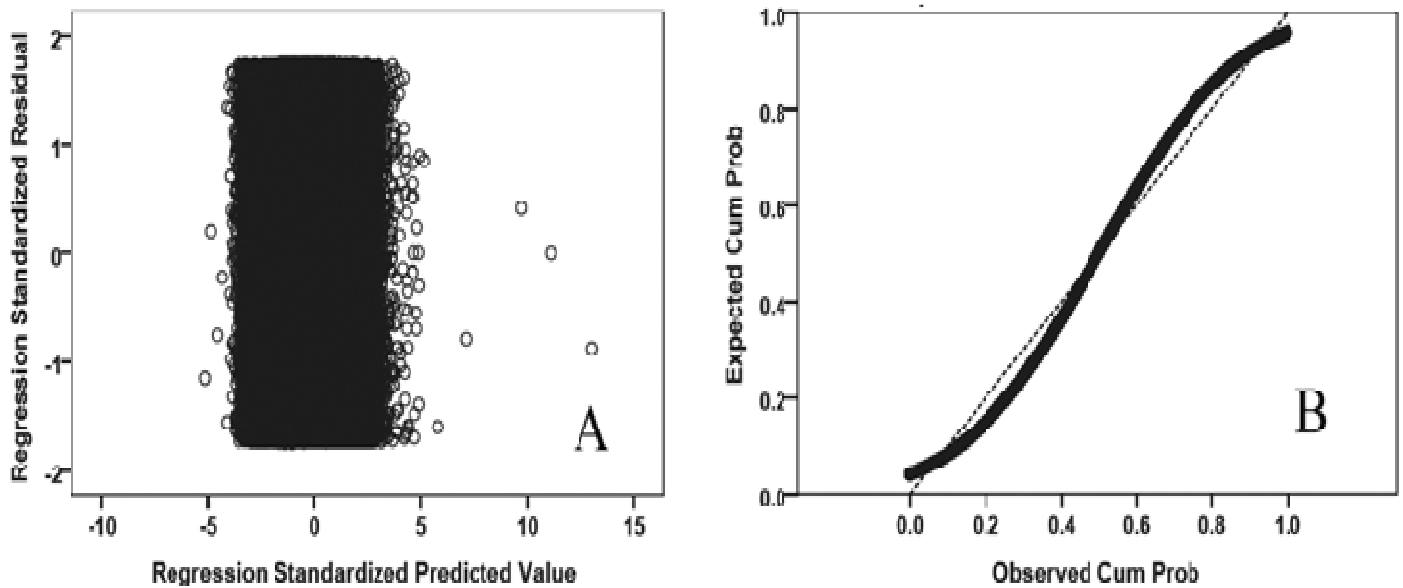
Figure 5. A scheme of two-stage wavelet-based image fusion method, discrete wavelet transfer (DWT) and inverse discrete Wavelet transfer (IDWT).

Table 4. R value, kernel size, modulation factor and center value for generation of high pass filter.

R Value	HPK Size	Center value			M
		Default value	Optional values		
$1 < R < 2.5$	5×5	24	28	32	0.25
$2.5 \leq R < 3.5$	7×7	48	56	64	0.50
$3.5 \leq R < 5.5$	9×9	80	93	106	0.50
$5.5 \leq R < 7.5$	11×11	120	150	180	0.65
$7.5 \leq R < 9.5$	13×13	168	210	252	1.0
$R \geq 9.5$	15×15	336	392	448	1.3

Table 5. Description statistics of Albedo as well as ASTER spectral bands acquired on day 186 of year 2000.

Layer	N	Minimum	Maximum	Mean	Standard deviation
ALBEDO	513608	0.1364	0.6057	0.2688	0.02578
B1	513608	0.0839	0.6647	0.2210	0.02851
B2	513608	0.0891	0.7578	0.2957	0.03821
B3	513608	0.1441	0.6798	0.3571	0.02612
B5	513608	0.2217	0.4573	0.3666	0.03814
B6	513608	0.2074	0.4681	0.3643	0.04278
B8	513608	0.1807	0.4309	0.3288	0.03149
B9	513608	0.2331	0.5111	0.3774	0.03708

**Figure 6.** (a) Residual scatter plot and (b) normal probability plot of regression standardized residual.

presented in Table 5.

Finally, downscaled high resolution image was calculated by following equation:

$$HighR_{Downscaled} = lowR + (HPF * W) \quad (14)$$

RESULTS AND DISCUSSION

Forward multiple regression

The description statistics of the data used for multiple regression analysis is as shown in Table 5.

The linearity of the relationship between DV and IV variables is realized visually from Figure 8. Preliminary data analysis approved the significant positive linear correlation ($R^2 > 0.9$) between spectral bands as well as Albedo at the 0.01 level. Inter-relation of the spectral bands also shows high level of correlation between bands 1 and 2 in visible-infrared and bands 5, 6 and 9 in

shortwave region (presence of collinearity). As shown in Table 6, correlation between band 1 of visible part with shortwave bands (B5, B6, B8 and B9) is also remarkable. In addition, as shown in Figure 7, a few numbers of values are far from the main cluster and it is associated with almost high value of shortwave bands. It should be noted that in remote sensing and energy balances application, decision about the removing of outliers is difficult since all land surface features must be considered and even some times prediction of a parameter for a feature is based on another, especially when they are associated with the highest and lowest value in the selected subset area. Thus, no action was taken until the determination of the most predictive spectral bands.

In order to verify the assumptions, normal probability plot and residual scatter plot were created via multiple regression practice. Regarding to normal probability plot (Figure 6b), all points are located along the straight diagonal line that certify the absence of the major deviation of variables from normality; although, slight

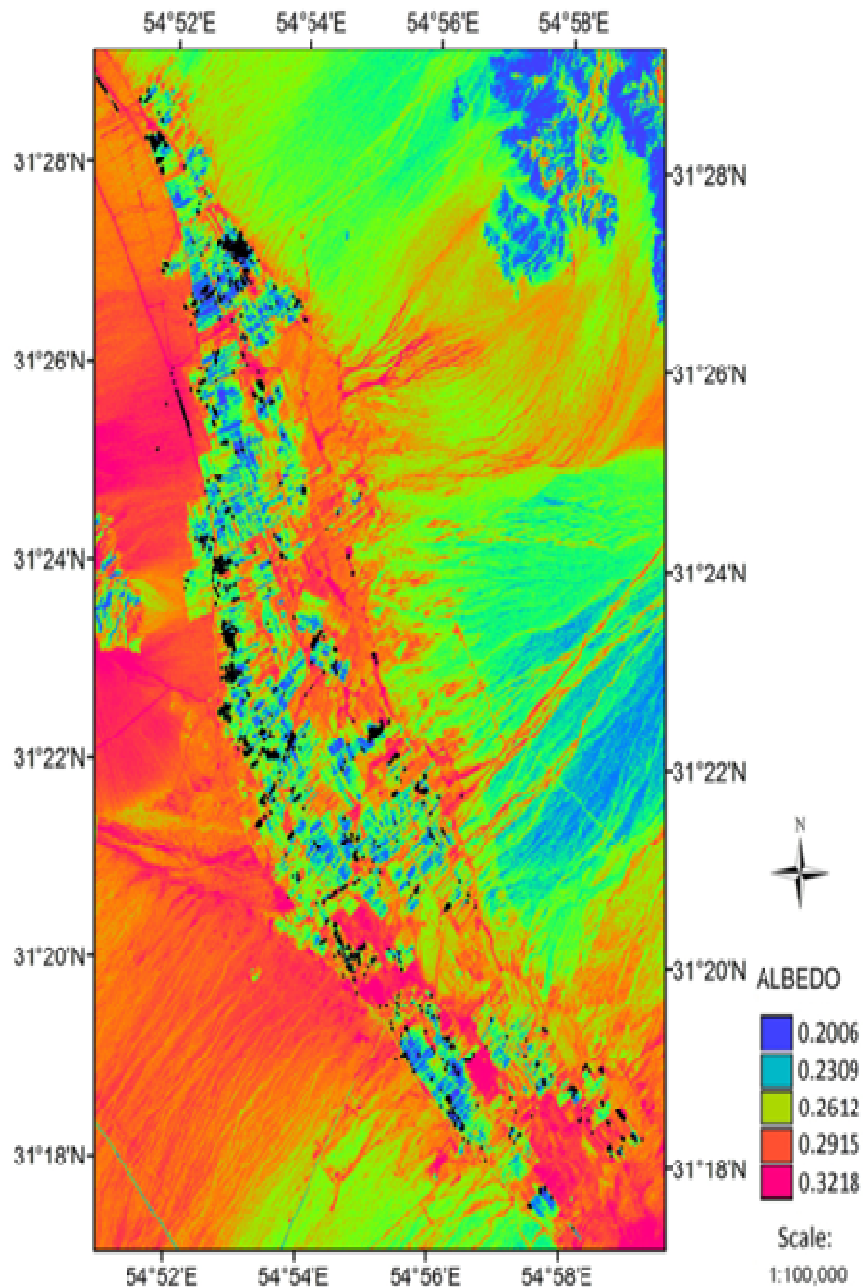


Figure 7. Occurrence of outliers (black speckles) in case of using 7 numbers of variables, day 186 of year 2000, pixel size = 15 m.

deviation from the line is observed. Nonlinearity assumption in this study is rejected since scatter plot shows points distributions in the form of rectangle (versus curved shape in case of nonlinearity). Moreover, each value of predicted score and a normal distribution of residuals formed well centralized rectangle and symmetrically from the center. Thus, in regard to Figure 6a, the high violation of the assumption was rejected, although, a few numbers of points as outliers was observed; Tabachnick and Fidell (2007) presented cut of

point value of ± 3.3 . Heteroscedasticity assumption is discarded as well, since the band enclosing width of the residuals becomes large at higher predicted value. Based on Mahalanobis distance test and Chi-square, (X^2) critical value of 24.32, at P value < 0.001 (Tabachnick and Fidell, 2007), 3325 points out of 513,608 (0.64%) were identified as outliers. These points are located, ranging from 0.20 to 0.32 of the estimated Albedo including vegetation and soil land covers (Figure 7).

Variance inflation factor (VIF) and tolerance indices

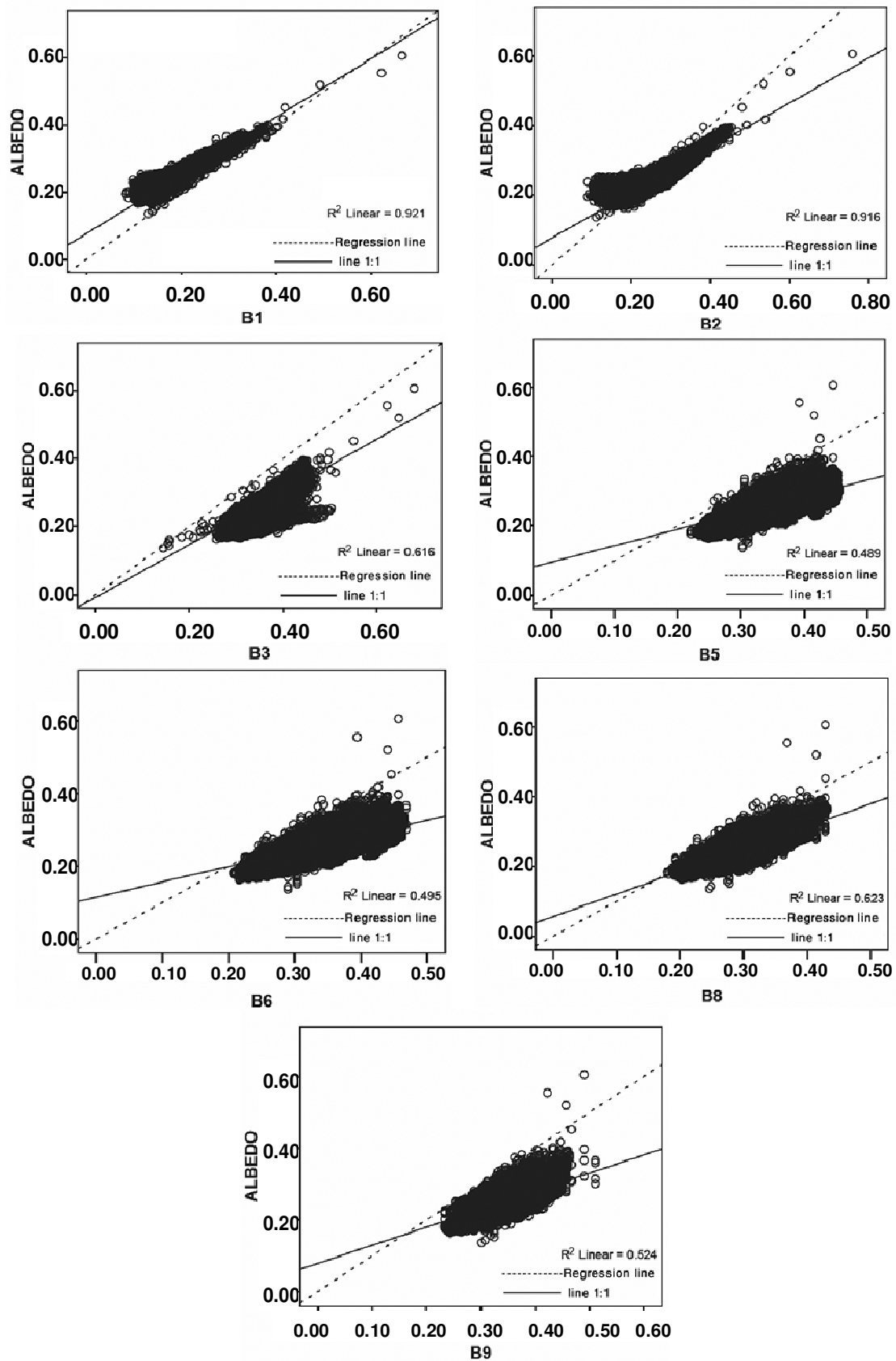


Figure 8. Scatter plot of Albedo estimated from Equation 1 and ASTER spectral bands (reflectance) acquired on day 186 of year 2000.

Table 6. Correlations matrix of Albedo and ASTER spectral bands, day 186 of year 2000.

	ALBEDO	B1	B2	B3	B5	B6	B8	B9
ALBEDO	1	0.960**	0.957**	0.785**	0.699**	0.704**	0.789**	0.724**
B1		1	0.972**	0.626**	0.751**	0.754**	0.805**	0.791**
B2			1	0.659**	0.710**	0.708**	0.808**	0.749**
B3				1	0.338**	0.325**	0.340**	0.286**
B5					1	0.994**	0.694**	0.957**
B6						1	0.700**	0.964**
B8							1	0.828**
B9								1

**Correlation (Pearson) is significant at the 0.01 level (2-tailed), $N = 513608$.

Table 7. Analysis of variances and proposed models for estimation of Albedo from ASTER bands.

	Model	Sum of squares	df	Mean square	F	Sig.
1	Regression	314.450	1	314.450	5968941.166	0.000 ^a
	Residual	27.057	513606	0.000	-	-
	Total	341.507	513607	-	-	-
2	Regression	333.446	2	166.723	10622468.684	0.000 ^b
	Residual	8.061	513605	0.000	-	-
	Total	341.507	513607	-	-	-
3	Regression	338.344	3	112.781	18313980.262	0.000 ^c
	Residual	3.163	513604	0.000	-	-
	Total	341.507	513607	-	-	-
4	Regression	338.494	4	84.623	14424357.140	0.000 ^d
	Residual	3.013	513603	0.000	-	-
	Total	341.507	513607	-	-	-
5	Regression	340.577	5	68.115	37625399.841	0.000 ^e
	Residual	0.930	513602	0.000	-	-
	Total	341.507	513607	-	-	-
6	Regression	341.506	6	56.918	6.844E10	0.000 ^f
	Residual	0.000	513601	0.000	-	-
	Total	341.507	513607	-	-	-

Model 1a: Predictors (Constant) band 1; Model 2b: Predictors (Constant) band 1 and 3; Model 3c: Predictors (Constant) band 1, 3 and 8; Model 4d: Predictors (Constant) band 1, 3, 8 and 6; Model 5: Predictors (Constant) band 1, 3, 8, 6 and 9; Model 6f: Predictors (Constant) band 1, 3, 8, 6, 9 and 5. Dependent variable: ALBEDO.

($1-R^2$) were used to investigate the presence of collinearity of independent variables in this study. In regard to the presented critical value of VIF (>10) and tolerance index (<0.1) for occurrence of multicollinearity (Pallant, 2007), band 3 with the tolerance of 0.402 has less collinearity with other independent variables and is followed by bands 8, 1 and 2 with the tolerance value of 0.11, 0.041 and 0.042, respectively. This can also be

roughly predicted from correlation matrix of variables in Table 6.

Table 7 illustrates the analysis of variances that resulted from forward regression method. Referring to this table, six number of model based on predictive potential of ASTER spectral bands were identified significantly at the 0.01 level. The zero value of standard error of regression for all models reveals that parameter

Table 8. The first three proposed models, coefficients and descriptive statistics.

Model		Unstandardized coefficient		Standardized coefficient	t	Sig.	R ²	Adjusted R ²	Standard error of the estimate
		B	Standard error	Beta					
1	Constant	0.077	0.000	-	972.564	0.000	0.921	0.921	0.007258
	B1	0.868	0.000	0.960	2443.142	0.000			
2	Constant	0.008	0.000	-	108.337	0.000	0.976	0.976	0.003961
	B1	0.696	0.000	0.770	2801.967	0.000			
	B3	0.299	0.000	0.302	1100.138	0.000			
3	Constant	-0.028	0.000	-	-450.739	0.000	0.991	0.991	0.002481
	B1	0.507	0.000	0.560	1922.070	0.000			
	B3	0.356	0.000	0.360	1958.116	0.000			
	B8	0.177	0.000	0.216	891.858	0.000			

Model-1 predictors: (Constant), Band 1; Model-2 predictors: (Constant), Band 1 and 3; Model-3 predictors: (Constant), Band 1, 3 and 8.

Table 9. The first three proposed models, coefficients and descriptive statistics.

Model		Unstandardized coefficients		Standardized coefficients	t	Sig.	R ²	Adj. R ²	Std. error of the estimate
		B	Std. Error	Beta					
1	Constant	0.077	0.000	----	972.564	0.000	0.921	0.921	0.007258
	B1	0.868	0.000	0.960	2443.142	0.000			
2	Constant	0.008	0.000	----	108.337	0.000	0.976	0.976	0.003961
	B1	0.696	0.000	0.770	2801.967	0.000			
	B3	0.299	0.000	0.302	1100.138	0.000			
3	Constant	-0.028	0.000	----	-450.739	0.000	0.991	0.991	0.002481
	B1	0.507	0.000	0.560	1922.070	0.000			
	B3	0.356	0.000	0.360	1958.116	0.000			
	B8	0.177	0.000	0.216	891.858	0.000			

Model- 1. Predictors: (Constant), Band 1

Model- 2. Predictors: (Constant), Band 1, Band 3

Model -3. Predictors: (Constant), Band 1, Band 3, Band 8

estimates are not varying from sample to sample.

Table 6 and Figure 8 indicate that surface Albedo is mostly accounted for by visible-near infrared part of ASTER spectral bands where land surface is covered by vegetation (pistachio) and soil, while shortwave bands are less correlated with Albedo. According to Table 7, if one IV is desired to be contributed in the model, Band 1 of the ASTER spectral data set is the choice that explains 92% of the variability of DV, Albedo. Using two variables, preferably bands 1 and 3 offered by forward regression analysis, 0.976% of variability of Albedo is accounted for

and if three independents variable is preferred to be included in the model, band 8 is the next option. In this case, these band combination account for 99% of variability of Albedo.

The corresponding coefficients of the first three proposed models are illustrated in Table 8. Band 6 as the fourth independent variable does not cover any variance of DV if bands 1, 3 and 8 are selected before hand in the model. However, in the case of unavailability of bands 5, 6, 8 and 9 (data acquired after April 2008), model 2 which is presented in Table 9 (constant bands 1 and 3) is the

option. It should be noted that band 2 has not been contributed to the models by this method since it is highly correlated with band 1 (0.972). If other bands are preferred to be contributed, bands 9, 8, 6 and 5 are proposed, respectively.

Moreover, statistical analysis of the models show that collinearity occurs when bands 6, 9 and 5 are added to model 3, respectively (Tolerance > 0.1 and VIF < 10). In term of collinearity analysis of the proposed models, band 3 has been identified to be less collinear with other bands.

Comparison of downscaling methods

The outputs of four downscaling methods were compared with the reference Albedo estimated from VNIR-SWIR bands (Equation 1). Evaluation of results was performed visually and statistically. Referring to Figure 9, all methods enhanced the spatial resolution with significant detail information as compared to the original MODIS Albedo image.

Overall impression and structure of PBIM and FSIM output is similar to the reference image (Figure 9B) while sharpness and blurred patterns can be visualized on HPF and wavelet method outputs, respectively. In addition, bright and dark features in FSIM image are smoother than image produced by PBIM method. Slight brightness difference associated with high Albedo value and brightness of the feature edges can be seen on HPF-based image fusion as compared to others. In addition, HPF-based downscaled image is seen to be noisy and highly textured in agricultural area as compared to two other methods.

The spectral preservation property of all downscaled images was also statistically analyzed. Tables 10 and 11 show descriptive statistic and correlation of the downscaled images, respectively. As shown in Table 10, the range ($valu_{max} - valu_{min}$) of the downscaled image by FSIM, PBIM and HPF are close to the range of reference image while the range of downscaled image by wavelet method is far from the reference image. In addition, FSIM has preserved maximum and minimum values close to the reference image, whereas these values were eliminated by wavelet method. However, outputs of all methods were highly correlated (significant at the 0.01 level) with reference image. As shown in Table 11, the correlation coefficient of 96, 95, 88 and 86 is related to SFIM, PBIM, wavelet and HPF methods, respectively which show a relatively higher performance of SFIM in downscaling image as compared to other methods. Liu (2000) also reported the higher performance of FSIM method over PBIM and wavelet. In summary, the FSIM method better improves both the spatial and spectral properties of the low spatial resolution image's features in this study, while spatial details were distorted mostly by Wavelet method.

Conclusion

The potential of ASTER visible-near infrared spectral bands in estimation of surface were considered in this study. The combination of bands 1 and 3 of ASTER spectral bands can effectively be modeled by regression method for determining surface Albedo instead of the six bands, with less than 0.024% loss of information, where land cover consists of vegetation and soil. Furthermore, the sum of the four omitted bands' from reference model (Equation 1) ranges (b5, b6, b8, b9), after applying their respective coefficients, is between 0.025 and 0.055; far less than the sum of the range of b3 and b1 in this case study. In other words, ASTER shortwave bands are less correlated with estimated Albedo as compares to visible-near infrared spectral bands in this area. However, collinearity is increased when bands 6, 9 and 5 are contributed in the model. Band number 2 is not recommended to be used in combination with two other visible-near infrared bands, since it is highly correlated with band 1 and causes collinearity. Based on the results, the forward multiple regression method and the generated new model, through this method, were identified to be a solution for the estimation of Albedo when the ASTER data acquired after April 2008 by missing bands number 4 through 9 were utilized. However, the results were significant in cases where the subset area consists of only vegetation and the soil is normally selected when the energy balance modeling in agricultural field is considered. Thus, the consistency of the generated models should be examined or the new coefficient should be determined when land cover is more heterogeneous and consist of several features. Moreover, this study was conducted in a representative semi-arid region. As such, application of VNIR-based Albedo estimation is suggested to be examined in areas with high variability of surface and atmospheric condition.

In addition, four downscaling methods including wavelet transfer, FSIM, PBIM and HPF methods were examined to downscale Albedo from MODIS 500 m resolution (pixel size based on short waves band) to aggregated 50 m ASTER Albedo image. VNIR-based Albedo image of ASTER data was used as high resolution image in the downscaling procedure. Downscaled images were validated against the Albedo estimated from the model presented by Liang (2004) which utilizes ASTER VNIR and SWIR bands. Visual interpretation confirms that boundaries between different land surface features were highlighted and the objects were discriminated clearly in downscaled images by all methods. Taking into account the statistical result, the correlation coefficient of the downscaled images confirmed that all methods improved the spatial and detailed information of the original MODIS data after downscaling. However, downscaled 50 m MODIS Albedo generated from FSIM method presents higher accuracy than the other methods with R^2 of 96 and RMES of 0.01. This highlighted better performance and relatively minimum

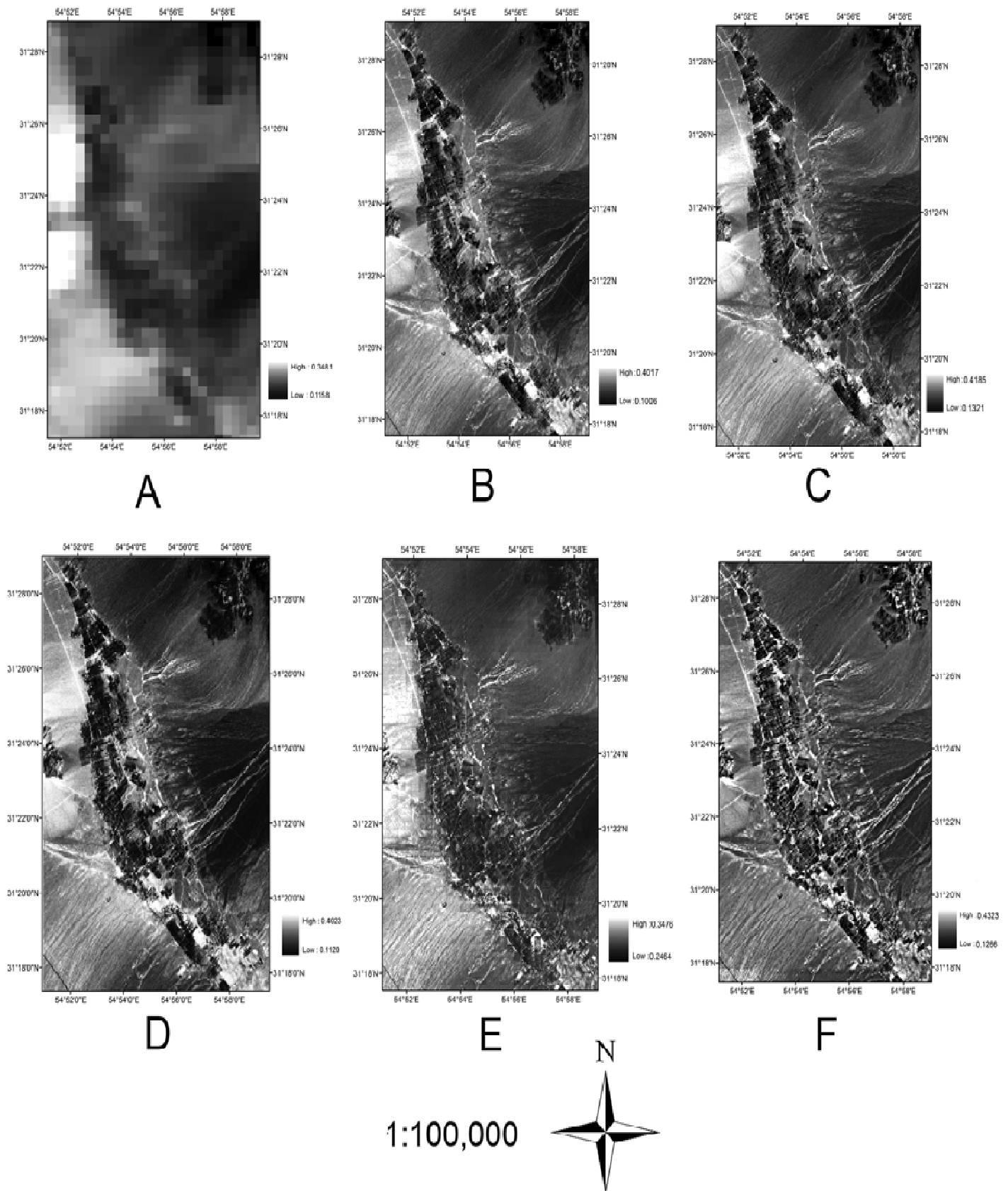


Figure 9. The downscaling results. (A) MODIS (500 m) Albedo image, (B) ASTER Albedo image, (C) downscaled MODIS image using PBIM method, (D) SFIM method, (E) Wavelet transfer method, and (F) HPF method.

Table 10. Descriptive statistics of downscaled images by three different methods.

Method	N	Minimum	Maximum	Range	St. deviation	Skewness		Kurtosis	
	Statistic	Statistic	Statistic	Statistic	Statistic	Statistic	St. error	Statistic	St. error
Albedo (eq.3)	123752	0.1006	0.4017	0.3011	0.02461	-0.105	0.007	0.300	0.015
SFIM	123752	0.1120	0.4023	0.2903	0.02293	-0.044	0.007	0.275	0.015
PBIM	123752	0.1321	0.4185	0.2864	0.02211	0.010	0.007	0.225	0.015
Wavelet	123752	0.2464	0.3476	0.1012	0.02074	0.713	0.007	-0.186	0.015
HPF	123752	0.1266	0.4323	0.3057	0.01540	-0.129	0.007	0.281	0.015

St = Standard.

Table 11. Statistical comparison of three downscaling methods.

Statistic	PBIM	SFIM	Wavelet	HPF
Root mean square error	0.0112	0.0101	0.0179	0.0168
Mean absolute error	0.0103	0.0100	0.0152	0.0137
Correlation coefficient	0.9509	0.9681	0.8838	0.8624

spectral distortion of FSIM as compared to other methods.

REFERENCES

- Abrams M (2000). The Advanced Spaceborne Thermal Emission and Reflection Radiometer ASTER: Data products for the high spatial resolution imager on NASA's Terra platform. *Int. J. Remote Sens.*, 21(5): 847-859.
- Benson BJ, MacKenzie MD (1995). Effects of sensor spatial resolution on landscape structure parameters. *Landscape Ecol.*, 10(2): 113-120.
- Bhattacharya BK, Mallick K, Padmanabhan N, Patel NK, Parihar JS (2009). Retrieval of land surface albedo and temperature using data from the Indian geostationary satellite: a case study for the winter months. *Int. J. Remote Sens.*, 30(12): 3239-3257.
- Bruno GD, Girel J, Chassery JM, Pautou G (1996). The use of Multiresolution Analysis and Wavelet transform for Merging SPOT Panchromatic and Multispectral Image data. *Photogramm. Eng. Rem. S.*, 62(9): 1057-1066.
- Burrus CS, Gopinath RA, Guo H (1998). Eds. *Introduction to Wavelets and Wavelet Transforms: A Primer*. Newjersey: Prentice Hall.
- Canty MJ, Nielsen AA, Schmidt M (2004). Automatic radiometric normalization of multitemporal satellite imagery. *Remote Sens. Environ.*, 91(3-4): 441-451.
- Congalton R (2010). *Remote Sensing: An Overview*. *Gisci Remote Sens.*, 47(4): 443-459.
- ERSDAC (2010). Earth Remote Sensing Data Analysis Center. <http://www.ersdac.or.jp/eng/index.E.html>.
- Folhes MT, Renn CD, Soares JV (2009). Remote sensing for irrigation water management in the semi-arid Northeast of Brazil. *Agr. Water Manage.*, 96(10): 1398-1408.
- Fujisada H, Ono A (1991). Overview of ASTER design concept, Proceedings Paper, Future European and Japanese Remote-Sensing Sensors and Programs, pp. 244-254.
- Gangkofner UG, Pradhan PS, Holcomb DW (2008). Optimizing the high-pass filter addition technique for image fusion. *Photogramm. Eng. Rem. S.*, 74(9): 1107-1118.
- Gonzalez RC, Woods RE, Eddins SL (2004). Eds. *Digital image processing using MATLAB*. New Jersey: Pearson Prentice Hall.
- Grant IF, Prata AJ, Cechet RP (2000). The impact of the diurnal variation of albedo on the remote sensing of the daily mean albedo of grassland. *J. Appl. Meteorol.*, 39: 231-244.
- Griffith JA, Stehman SV, Sohl TL, Loveland TR (2003). Detecting trends in landscape pattern metrics over a 20-year period using a sampling-based monitoring programme. *Int. J. Remote Sens.*, 24(1): 175-181.
- Guo LJ, Moore JM (1998). Pixel block intensity modulation: Adding spatial detail to TM band 6 thermal imagery. *Int. J. Remote Sens.*, 19(13): 2477-2491.
- Gupta RV (2003). Eds. *Remote Sensing Geology: Second ed.* Berlin, Germany, Springer.
- Haydan R, Dalke GW, Henkel J, Bare JE (1982). *Int Symp Remote Sens. of Arid and Semi-arid Lands*, Cairo, Egypt. pp. 599-616.
- Hong SH, Hendrickx JMH, Borchers B (2009). Up-scaling of SEBAL derived evapotranspiration maps from LANDSAT (30 m) to MODIS (250 m) scale. *J. Hydrol.*, 370(1-4): 122-138.
- Huang J, Chen D, Cosh MH (2009). Sub-pixel reflectance unmixing in estimating vegetation water content and dry biomass of corn and soybeans cropland using normalized difference water index (NDWI) from satellites. *Int. J. Remote Sens.*, 30(8): 2075-2104.
- Kaheil YH, Rosero E, Gill MK, McKee M, Bastidas LA (2008). Downscaling and Forecasting of Evapotranspiration Using a Synthetic Model of Wavelets and Support Vector Machines. *IEEE Geosci. Remote S. on*, 46(9): 2692-2707.
- Kimes DS, Sellers PJ (1985). Inferring hemispherical reflectance of the earth's surface for global energy budgets from remotely sensed nadir or directional radiance values. *Remote Sens. Environ.*, 18(3): 205-223.
- King RL, Jianwen W (2001). A wavelet based algorithm for pan sharpening Landsat 7 imagery. In: *Geosci Remote S Symp. IGARSS '01. IEEE 2001 International*, 2: 849-851.
- Kojima N, Laba M, Velez Liendo XM, Bradley AV, Millington AC, Baveye P (2006). Causes of the apparent scale independence of fractal indices associated with forest fragmentation in Bolivia. *Isprs J. Photogramm.*, 61(2): 84-94.
- Kustas WP, Perry EM, Doraiswamy PC, Moran MS (1994). Using satellite remote sensing to extrapolate evapotranspiration estimates in time and space over a semiarid Rangeland basin. *Remote Sens. Environ.*, 49(3): 275-286.
- Liang S, Shuey CJ, Russ AL, Fang H, Chen M, Walthall CL, Daughtry CST, Hunt R (2003). Narrowband to broadband conversions of land surface albedo: II. Validation. *Remote Sens. Environ.*, 84(1): 25-41.
- Liu JG (2000). Smoothing Filter-based Intensity Modulation: a spectral preserve image fusion technique for improving spatial details. *Int. J. Remote Sens.*, 21(18): 3461-3472.
- Ozdogan M (2009). The spatial distribution of crop types from MODIS data: Temporal unmixing using Independent Component Analysis. *Remote Sens. Environ.*, 114(6): 1190-1204.
- Pallant J (2007). Eds. *SPSS, Survival Manual, A Step by Step Guide to*

- Data Analysis using SPSS for Windows third ed: McGraw-Hill.
- Pardo-Iguzquiza E, Atkinson PM (2007). Modelling the semivariograms and cross-semivariograms required in downscaling cokriging by numerical convolution-deconvolution. *Comput. Geosci.*, 33(10): 1273-1284.
- Pardo-Iguzquiza E, Atkinson PM, Chica-Olmo M (2009). DSCOKRI: A library of computer programs for downscaling cokriging in support of remote sensing applications. *Comput. Geosci.*, 36(7): 881-894.
- Pardo-Iguzquiza E, Chica-Olmo M, Atkinson PM (2006). Downscaling cokriging for image sharpening. *Remote Sens. Environ.*, 102(1-2): 86-98.
- Pinker RT, Stowe LL (1990). Modelling planetary bidirectional reflectance over land. *Int. J. Remote Sens.*, 11(1): 113-123.
- Ranchin T, Aiazzi B, Alparone L, Baronti S, Wald L (2003). Image fusion - The ARSIS concept and some successful implementation schemes. *Isprs J. Photogramm.*, 58(1-2): 4-18.
- Ranson KJ, Irons JR, Daughtry CST (1991). Surface albedo from bidirectional reflectance. *Remote Sens. Environ.*, 35(2-3): 201-211.
- Ricchiuzzi P, Yang S, Gautier C, Sowle D (1998). SBDART: A Research and Teaching Software Tool for Plane-Parallel Radiative Transfer in the Earth's Atmosphere. *B Am. Meteorol. Soc.*, 79(10): 2101-2114.
- Saura S (2004). Effects of remote sensor spatial resolution and data aggregation on selected fragmentation indices. *Landscape Ecol.*, 19(2): 197-209.
- Saura S, Castro S (2007). Scaling functions for landscape pattern metrics derived from remotely sensed data: Are their subpixel estimates really accurate? *Isprs J. Photogramm.*, 62(3): 201-216.
- Schaaf CB, Gao F, Strahler AH, Lucht W, Li X, Tsang T, Strugnell NC, Zhang X, Jin Y, Muller JP, Lewis P, Barnsley M, Hobson P, Disney M, Roberts G, Dunderdale M, Doll C, D'Entremont RP, Hu B, Liang S, Privette JL, Roy D (2002). First operational BRDF, albedo nadir reflectance products from MODIS. *Remote Sens. Environ.*, 83(1-2): 135-148.
- Shi W, Zhu C, Tian Y, Nichol J (2005). Wavelet-based image fusion and quality assessment. *Int. J. Appl. Earth Obs.*, 6(3-4): 241-251.
- Shi W, Zhu C, Yang X (2003). Multi-band wavelet for fusing SPOT panchromatic and multispectral images. *Photogramm Eng. Rem. S.*, 69(5): 513-520.
- Stathopoulou M, Cartalis C (2009). Downscaling AVHRR land surface temperatures for improved surface urban heat island intensity estimation. *Remote Sens. Environ.*, 113(12): 2592-2605.
- Strang G, Nguyen T (1996). Eds. *Wavelets and Filter Banks* Wellesley-Cambridge Press.
- Tabachnick BG, Fidell LS (2007). Eds. *Using Multivariate Statistics*. Fifth ed. Boston: Pearson Education.
- Wang Q, Tenhunen J, Dinh NQ, Reichstein M, Vesala T, Keronen P (2004). Similarities in ground- and satellite-based NDVI time series and their relationship to physiological activity of a Scots pine forest in Finland. *Remote Sens. Environ.*, 93(1-2): 225-237.
- Yocky DA (1996). Multiresolution wavelet decomposition image merger of LANDSAT Thematic Mapper and SPOT panchromatic data. *Photogramm Eng. Rem. S.*, 62(9): 1067-1074.
- Yu X, Ng C (2006). An integrated evaluation of landscape change using remote sensing and landscape metrics: A case study of Panyu, Guangzhou. *Int. J. Remote Sens.*, 27(6): 1075-1092.
- Zaksek K, Schroedter-Homscheidt M (2009). Parameterization of air temperature in high temporal and spatial resolution from a combination of the SEVIRI and MODIS instruments. *Isprs J. Photogramm.*, 64(4): 414-421.
- Zurita-Milla R, Kaiser G, Clevers JGPW, Schneider W, Schaepman ME (2009). Downscaling time series of MERIS full resolution data to monitor vegetation seasonal dynamics. *Remote Sens. Environ.*, 113(9): 1874-1885.